

MASTER THESIS

---

**PROBING THE CORRELATION  
BETWEEN IR AND X-RAY EMISSION IN  
LUMINOUS INFRARED GALAXIES**

---

July 3, 2015

**Author:**

Núria Torres Albà

**Advisor:**

Kazushi Iwasawa

**Tutor:**

Valentí Bosch Ramon

Universitat de Barcelona  
Dept. d'Astronomia i Meteorologia

## Acknowledgement

I would like to thank my advisor, Kazushi Iwasawa, for all the help and guidance provided throughout all these months. His extensive knowledge and experience on the field of study has been crucial for this work's development, providing me with a proper understanding of the subject.

I would also like to thank my tutor, Valentí Bosch-Ramon, for his counselling and direction in the final theoretical development, as well as his advice and revisions.

In addition, I also thank Josep Maria Paredes for the final comments and suggestions, helping in the improvement of this work's clarity.

## Abstract

In this work, X-ray data for a sample of 59 luminous infrared galaxies (LIRGs), obtained with the Chandra X-ray Observatory is presented. These are observations of the lower luminosity portion of the Great Observatory All-sky LIRG Survey (GOALS), which includes the most luminous infrared selected galaxies,  $\log(L_{ir}/L_{\odot}) \geq 11.05$ , in the local universe,  $z \leq 0.088$ . With combined X-ray and mid infrared diagnostics for AGN, AGN are found in 32 % of the objects. Objects without traces of AGN appear to be underluminous in X-rays, compared to the previously derived far infrared and X-ray correlations for starburst galaxies at lower star formation rates. Our results suggest the previous claim that star formation rate can be directly inferred from X-ray luminosity may not hold for dusty galaxies like LIRGs.

# Contents

<b>1</b>	<b>Introduction</b>	<b>5</b>
1.1	Luminous infrared galaxies (LIRGs) . . . . .	5
1.1.1	Origin of the infrared emission . . . . .	5
1.1.2	Merger: Origin of AGN and starburst . . . . .	6
1.2	X-ray study . . . . .	7
1.2.1	The X-ray spectrum of an AGN . . . . .	7
1.2.2	The X-ray spectrum of a starburst region . . . . .	8
<b>2</b>	<b>X-ray observations</b>	<b>10</b>
2.1	Chandra and XMM-Newton . . . . .	11
<b>3</b>	<b>GOALS</b>	<b>12</b>
<b>4</b>	<b>Chandra observations of LIRGs</b>	<b>12</b>
4.1	The sample . . . . .	12
4.2	Observations and data reduction . . . . .	13
4.2.1	Hard band fitting . . . . .	16
4.2.2	Soft band fitting . . . . .	16
4.2.3	Special cases . . . . .	17
4.3	Results . . . . .	18
4.3.1	AGN selection . . . . .	18
4.3.2	X-ray luminosities and correlation with IR . . . . .	20
<b>5</b>	<b>Discussion</b>	<b>24</b>
5.1	X-ray and infrared luminosity correlation . . . . .	24
5.2	Molecular disk and AGN interaction . . . . .	26

# 1 Introduction

In astronomy, many methods are used to estimate the star formation rate in galaxies, as described in a review by Kennicutt (1998), the basis of which are different manners of quantifying the amount of hot, young, and short-lived stars. One of these methods is a measurement of the energy deposited in the dust of the interstellar medium by these stars, which is obtained through far-infrared luminosity measurements. Therefore, far-infrared luminosity can be directly related to the star formation rate, and is probably the best method to determine it.

In galaxies with a considerable amount of star formation, such as starburst galaxies, emission in other wavelengths can be somewhat related to young and massive stars, such as X-ray luminosity (e.g. X-ray binaries emission, supernova remnants (SNRs)). Therefore, it has been suggested that if a good correlation between X-ray luminosity and IR luminosity exists in galaxies, the star formation rate (SFR) can be directly inferred from the X-ray luminosity (e.g. Ranalli *et al.*, 2003; Grimm *et al.*, 2003; Mineo *et al.*, 2014). However, the applicability of this method has been questioned due to experimental results at higher SFRs (e.g. Iwasawa *et al.*, 2009). The aim of this work is the study of this correlation through the calculation of the X-ray luminosity derived from Chandra spectral data in a subsample of GOALS galaxies, in order to further constrain its usability.

## 1.1 Luminous infrared galaxies (LIRGs)

Luminous infrared galaxies (LIRGs) are galaxies with an infrared luminosity between  $10^{11}L_{\odot}$  and  $10^{12}L_{\odot}$ , emitting more in this band than in all other bands combined. Galaxies with an even higher infrared luminosity, above  $10^{12}L_{\odot}$  are called ULIRGS, Ultra Luminous Infrared Galaxies.

### 1.1.1 Origin of the infrared emission

Galaxies emit in the infrared mainly through three sources: stars, interstellar gas and dust. The emission from stars peaks in the near infrared (1-3 microns), and the emission from atoms and molecules in the interstellar gas makes up only a few percent of the total infrared luminosity in galaxies. Dust is heated by starlight and emits thermally, clearly being the dominating infrared source beyond 3 microns.

The reason some galaxies emit more in the infrared than others is due to a high increase in the dust emission, which is due to an increase in the amount of energetic photons coming from the sources that heat this dust. As dust absorbs preferentially UV emission, since the cross-section is highest for UV light, most of the absorbed photons will come from the massive O and B stars. Another important contribution to the dust heating is the continuum emission from an active nuclei's accretion disk, as it peaks in the far UV.

Therefore, the high infrared luminosity in LIRGs may come from both an ex-

tremely high star formation rate, which is known as starburst, giving rise to many young luminous stars, and the contribution of an active galactic nuclei (AGN) component.

### 1.1.2 Merger: Origin of AGN and starburst

When cool gas is available in a galaxy it settles in a disk-like morphology to conserve angular momentum. As this configuration is stable, there is need of a merger in order to funnel it towards the central regions of a galaxy, where it can feed both star formation and the central black hole, thus both processes being somewhat correlated.

Kauffman *et al.* (2003a) found that low-luminosity AGN rather live in galaxies with older stellar populations, while the high-luminosity ones tend to be hosted by galaxies with young populations. In fact, strong  $H\delta$  absorption lines in high-luminosity sources indicate that these galaxies have experienced a starburst some 0.1-1 Gyr ago, and tracers of starburst tend to correlate with AGN activity indicators (e.g. Schweitzer *et al.*, 2006).

Silverman *et al.* (2009) studied the hosts of 147 Chandra detected AGN, which appear to preferentially be inside environments with substantial star formation. The same conclusion was reached by Rumbaugh *et al.* (2012), finding that on average AGN hosts either are still active starburst galaxies or have experienced one within the previous  $\sim 1$  Gyr.

However, AGN and star formation processes do not necessarily end at the same time: the mass involved in an active star formation phase is some hundreds to thousand of times larger than the mass accreted onto the black hole. Therefore, once the starburst dies out, AGN activity can continue. As the galaxy is more and more depleted of gas, even the black hole's activity comes to a halt, entering a quiescent stage. It is believed that all galaxies, now known to host a supermassive central black holes, have once gone through both a period of strong activity and a high star formation rate. Therefore, the study of these starburst galaxies can significantly contribute to the understanding of galaxy evolution.

Another key point derived from the study of these type of galaxies is galaxy building, since more than 95% of ULIRG sources are mergers (Sanders and Mirabel, 1996). The current favoured model for the building up is hierarchical growth, which is based on the idea that galaxies form mainly through the merging of nearby smaller galaxies to give rise to larger structure, which will then undergo further merging. Sanders (1999) thus puts the ULIRGs as a stage or episode between gas-rich merging disk galaxies and the resulting ellipticals. Both cosmological simulations and observation of large scale structure, which becomes more pronounced towards lower redshifts, support this theory.

In more than 70% of the cases, AGN host galaxies have nearby companions, some showing tidal tails, which are strong evidence for interaction (Beckmann and Shrader, 2012). These tidal forces can, prior to the merger per se, lead to a distur-

bance, which allows matter to flow into the centre towards the black hole, as well as triggering star formation in the galaxies due to compression of gas. After a major merger, most of the cold gas is driven to the core of the galaxies' remnant and this large in-flow of gas can feed or trigger these starburst and AGN processes.

If an efficient mass intake takes place, the SFR and black hole growth accelerate rapidly, within a few  $10^8$  years. Based on simulations of the AGN activation through major merging events, Hopkins et al. (2005) derive a black hole growth time scale of about  $\sim 100$  Myr. The AGN will be active throughout this time, but surrounded by obscuring material, and thus will appear dim. Most of the accretion would occur during this obscured phase, which would end with the clearing of the surrounding material, probably due to the AGN's own activity (heating of the surrounding gas, expulsion due to strong winds or jets...), and the natural depletion of gas after being consumed. Afterwards, the object will appear as a bright quasar for a duration of  $\sim 10$  Myr, before exhausting completely its fuel and returning to a quiescent state (Sanders, 1999).

## 1.2 X-ray study

Both the AGN and starburst component in a LIRG are observed in a large range of wavelengths, from radio to high energies. Electromagnetic radiation between  $\sim 120$  eV and  $\sim 120$  keV, associated to thermal temperatures above  $10^7$  K, is referred to as X-rays. The study of radiation in this domain has seen an enormous evolution over recent decades, and is currently one of the key energy ranges to study AGN.

X-ray photons have low extinction cross section in the ISM, therefore X-ray observations are much less vulnerable to dust extinction than optical or UV observations. Chandra observations routinely penetrate  $A_V > 100$  mag of optical extinction (Wang, 2007).

Therefore, in order to study such highly obscured galaxies, X-ray emission is particularly adequate. Also, AGN are the dominating sources of cosmic X-rays: in any medium-deep image of the X-ray sky at high galactic latitudes, the majority of detections (about 80%, Gandhi, 2005) are AGN.

### 1.2.1 The X-ray spectrum of an AGN

X-rays are the most direct probe of the accretion processes responsible for such high energy emission, as they can penetrate through large columns of obscuring gas and dust.

Accreting matter falls towards the black hole, settling in a planar orbit around it, where gravitational energy is released through dissipation. Temperature increases in the disk when approaching the central engine, reaching the X-ray generating temperatures at a few gravitational radii from it, producing a thermal spectrum. The low-energy photons produced are scattered through inverse Compton to higher energies by relativistic electrons in the corona (Haardt and Maraschi, 1993). The

inverse Compton spectrum has a power law shape with a photon index of  $\Gamma \simeq 2$ , and as the disk temperature and the electron energies are limited, it has a high energy cutoff.

Superposed to this powerlaw, reflection of photons from the corona leads to the appearance of a hump in the hard X-ray spectrum, generally peaking at around 20–30 keV, where the reflection efficiency has its maximum. Another signature of the reflection process is the  $^{26}\text{Fe}K_{\alpha 1}$  fluorescence line at  $E_{K_{\alpha}} = 6.404$  keV. A representation of the resulting spectrum can be seen in Fig. 1.

The origin of reflection is theorized to be caused by a cold, optically-thick material. As X-ray continuum illuminates the material, photons can either be Compton scattered by free or bound electrons or they can be absorbed, followed by fluorescent line emission (George and Fabian, 1991). The origin of the soft excess emission is still an open issue (Dewangan *et al.*, 2007; Crummy *et al.*, 2006; Done, 2007)

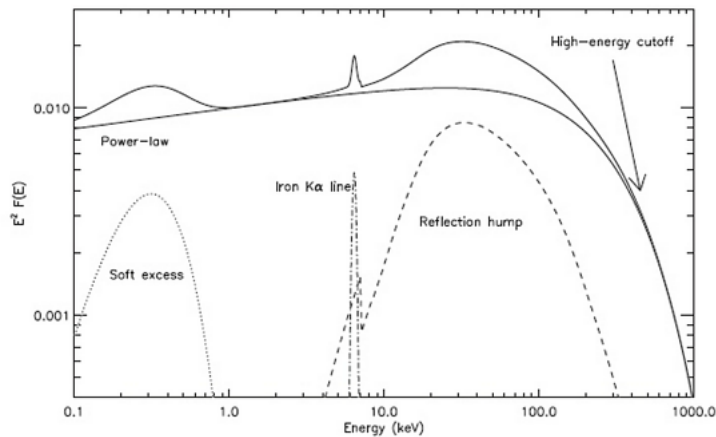


**Figure 1:** Schematic representation of a type 1 AGN spectrum in the X-ray. Image from Ricci (2012).

AGN are classified into type 1 or type 2 based on the measurement of intrinsic absorption in the X-ray band. The lower energy spectrum of an AGN (below 10 keV) is modified by obscuring gas through photoelectric absorption if the line of sight passes through the obscuring torus. At a column density of  $N_H \sim 1.5 \cdot 10^{24} \text{cm}^{-2}$  the energy transmitted at 10 keV decreases one e-folding, being these sources called Compton-thick. At higher column densities, multiple scatterings, as modelled by the Klein-Nishina cross section, lead to a Compton down-scattering over the full X-ray regime. At column densities of about  $N_H \gg 1.5 \cdot 10^{24} \text{cm}^{-2}$ , barely any flux emerges (Fig. 2), as all photons are scattered more than once.

### 1.2.2 The X-ray spectrum of a starburst region

An enhanced star formation rate comes with an increase of the energetic phenomena associated with the final stages of stellar evolution: X-ray binaries, supernova remnants (SNRs), galactic winds and, it has been predicted though still not ob-

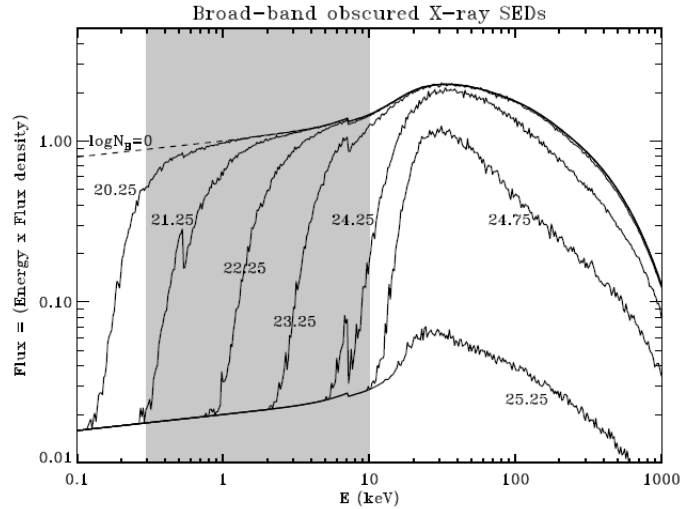


**Figure 2:** Modelled AGN rest-frame X-ray spectral energy distributions, showing intrinsic power law emission, reflection effects and high energy exponential cut-off. Obscuration by material is presented for different column densities, labelled as  $\log[N_H] = 20.25$  to  $25.25$ , in units of  $\text{atoms cm}^{-2}$ . The shaded region marks the X-ray spectral regime that is accessible for study to current high spatial resolution X-ray instruments such as Chandra and XMM-Newton. Figure from Gandhi (2005).

served, Compton scattering of ambient FIR photons by SN-accelerated relativistic electrons (for a more detailed description, refer to Persic and Rephaeli (2002)). A typical starburst spectrum (as the one shown in Fig. 3) has the following main contributions:

- Binary systems are the brightest galactic X-ray sources, and it is generally assumed that they dominate the emission in starburst galaxies in the range of 2–10 keV. The high-mass X-ray binaries (HMXB) are formed by a neutron star or a black hole and an optical companion of  $M_{opt} \geq 8M_{\odot}$ . X-ray emission comes from the accretion by the massive compact object of matter driven by the high mass star’s wind. This generates a powerlaw spectra of photon index  $\Gamma \simeq 1.2$ , so harder than that of a typical AGN. A striking characteristic in the HMXB spectra is a prominent Fe-K emission feature with central energy in the range 6.4–6.7 keV, generated in the companion’s stellar wind or in the compact object’s magnetosphere.
- Massive stars, with  $M \geq 8M_{\odot}$ , will end up exploding as supernovae. X-ray emission from this sources comes mainly from the first phase of evolution of the SNR, the free expansion, as its material shocks and sweeps the surrounding ISM and heats gas. This results in a thermal spectrum with  $kT \sim 2$  keV, coming primarily from bremsstrahlung continuum and collisionally excited lines, one of which can be the mentioned intense Fe-K line. A contribution of non-thermal emission may also be present, coming from the central pulsar, or from

synchrotron emission by electrons accelerated in the shock.

- The high SN rate in a starburst implies an increase in relativistic electron densities, as SN shocks are important sites of cosmic ray acceleration. These relativistic electrons can Compton up-scatter low energy FIR photons, abundant in a starburst region as previously explained, to hard X-ray energies, resulting in a powerlaw spectrum with the photon index of the electron population.
- An important contribution in the softer X-ray emission is that coming from more external ISM and the galactic halo gas, shock-heated by the multiple SN explosions and stellar winds, with  $kT \lesssim 1$  keV. Thermal soft X-ray emission is therefore expected from this gas.

As all these contributions are directly related to the star formation, in starburst regions X-ray luminosity can be related to the star formation rate.

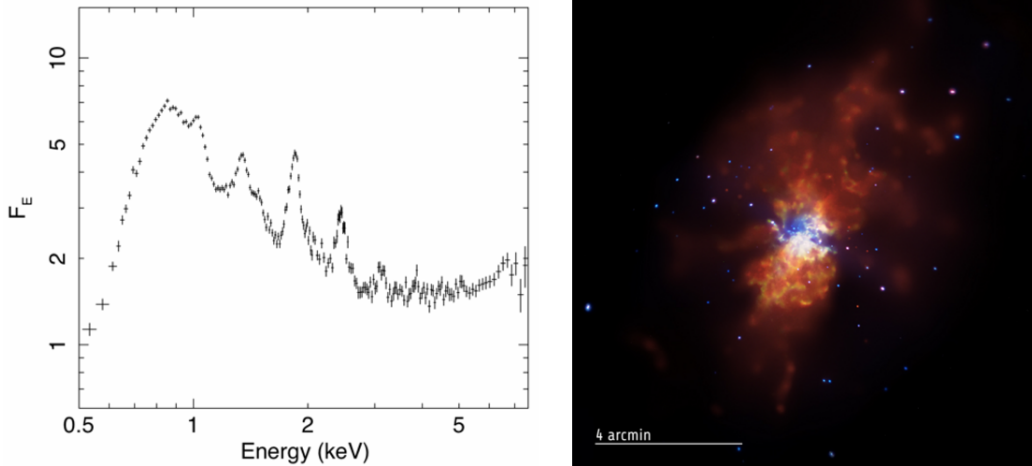


**Figure 3:** XMM-Newton spectrum of galaxy M82 (K. Iwasawa, private communication), typical starburst, with multiple emission lines and a hard tail (left). X-ray image of M82 (right, Chandra photo album: January 13, 2011.). Red: 0.3–1.1 keV, Green: 0.7–2.2 keV, Blue: 2.2–6 keV. Resolved point sources are X-ray binaries.

## 2 X-ray observations

Unlike modern optical astronomy, which began about 400 years ago with the use of the first telescopes, X-ray astronomy is only about four decades old. The main reason for this late development is the high opaqueness of the atmosphere to X-rays, due to the high photoelectric absorption cross-section of this energetic photons in air. The second reason is that the very small wavelengths at such high energies require new ways to focus light in order to form images.

The first of these two problems implies the necessity of performing X-ray observations in space, with the use of artificial satellites.

The second difficulty arises from the fact that X-ray photons typically have energies 1000 times higher than that of optical photons. Thus, normal incidence mirrors generally used to focus optical light completely absorb X-rays, making it impossible to use the well known telescope techniques in optical regime.

To focus X-rays, two conditions are necessary. The first one is for the incidence angle to be very small, in order to avoid absorption of the photons. This reflection angle varies as  $\sqrt{\rho}/E$ , where  $\rho$  is the density of the reflecting surface and  $E$  the energy of the incoming X-ray photon (Aschenbach, 1985). Thus, the higher this energy, the smaller the angle has to be in order to obtain reflection. For photons of a few keV, this angle turns out to be smaller than  $1^\circ$ .

The second requirement is that the reflecting surface has to be highly polished, to an average roughness of only a few angstroms, given the small reflection angles and photon wavelengths. Alignment, polishing and coating of the mirror surfaces are the most critical parts of the assembly.

Therefore, X-ray mirrors are highly polished surfaces placed almost parallel to the incoming beam. The reflection of a paraboloid section followed by a confocal and coaxial hyperboloid surface provides good focus on-axis and also at a small off-axis angles (about a few arcmin at most), as seen in Fig.4. As the mirrors are placed in the direction of the incoming light, the effective surface of reflection is very small, and thus the sensitivity is low. To solve this, the reflecting area is increased by nesting concentric surfaces of different radii.

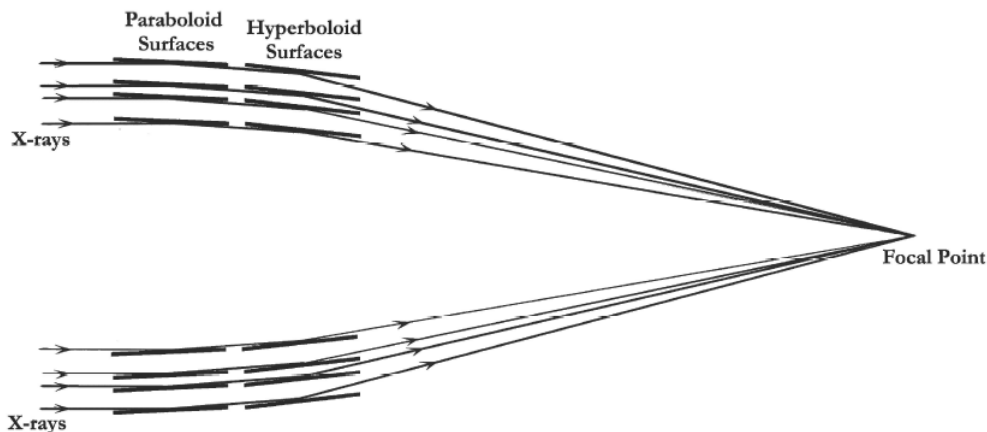


**Figure 4:** Main elements of a Wolter type 1 nested X-ray focusing mirror configuration. Image from <http://chandra.harvard.edu/>.

## 2.1 Chandra and XMM-Newton

Two major observatories were launched in 1999: NASA's Chandra satellite and ESA's XMM-Newton mission.

Chandra has four pairs of iridium-coated mirrors, the largest one with a diameter of 120 cm. Depending on the wavelength, the effective area ranges from  $800 \text{ cm}^2$

to  $40 \text{ cm}^2$ , being the lower value for the shortest wavelengths. Its focal length is of 10 m. Chandra’s best feature is that it allows an incredibly good spatial resolution, of 0.5 arcsec, the best of any X-ray instrument ever built. Its observation range is from 0.1 to 10 keV.

XMM Newton is comprised of 3 X-ray telescopes, each consisting of 58 nested mirrors coated with gold, the biggest of which has a diameter of 70 cm. Its focal length is of 7.5 m, and the effective area ranges from  $1900 \text{ cm}^2$  at low energies to  $350 \text{ cm}^2$  at high energies. It complements Chandra by having a much larger collecting area, but a worse spatial resolution by a factor of a few. It is able to search for spectral features in distant cosmic sources fainter than those detectable by any previous mission.

### 3 GOALS

The Great Observatories All-sky LIRG Survey (GOALS, Armus *et al.*, 2009), is combining imaging and spectroscopic data from NASA’s Spitzer, Hubble, Chandra and GALEX space-borne observatories in a comprehensive study of over 200 of the most luminous infrared-selected galaxies in the local Universe. The sample consists of approximately 180 LIRGs as well as over 20 ULIRGs, 77 of which are systems that contain multiple galaxies. The objects are a complete subset of the IRAS Revised Bright Galaxy Sample (RBGS, Sanders *et al.*, 2003), which comprises 629 extragalactic objects with 60-micron flux densities above 5.24 Jy and Galactic latitude above five degrees. The RBGS objects, all with redshifts,  $z < 0.088$ , are the brightest 60-micron sources in the extragalactic sky. The LIRGs and ULIRGs targeted in GOALS span the full range of nuclear spectral types (type-1 and type-2 AGN, LINERs, and starbursts) and interaction stages (major mergers, minor mergers, and isolated galaxies). They provide an unbiased picture of the processes responsible for enhanced infrared emission in the local Universe, and are excellent analogues for comparisons with infrared and sub-millimetre selected galaxies at high-redshift.

## 4 Chandra observations of LIRGs

### 4.1 The sample

The sample studied in this work consists of 59 systems from the GOALS sample, 15 of which contain multiple galaxies. It represents the low luminosity part of the GOALS sample, with  $11.05 \leq \log(L_{ir}/L_{\odot}) \leq 11.73$ , incomplete as Chandra data for all systems is unavailable. The redshift range is  $z = 0.003 - 0.037$ . The median IR luminosity of the sample is  $\log(L_{ir}/L_{\odot}) = 11.40$ , corresponding to  $\log(L_{ir}) = 44.99$ . Table 1 gives basic data for all 59 systems in the sample.

A complete study of the high luminosity part,  $11.73 \leq \log(L_{ir}/L_{\odot}) \leq 12.57$ , with

44 systems, was carried out by Iwasawa *et al.* (2011), with  $z = 0.010 - 0.088$  and median  $\log(L_{ir}/L_{\odot}) = 11.99$ , corresponding to  $\log(L_{ir}) = 45.58$ . A comparison of the properties of the two samples is shown in Fig. 5.

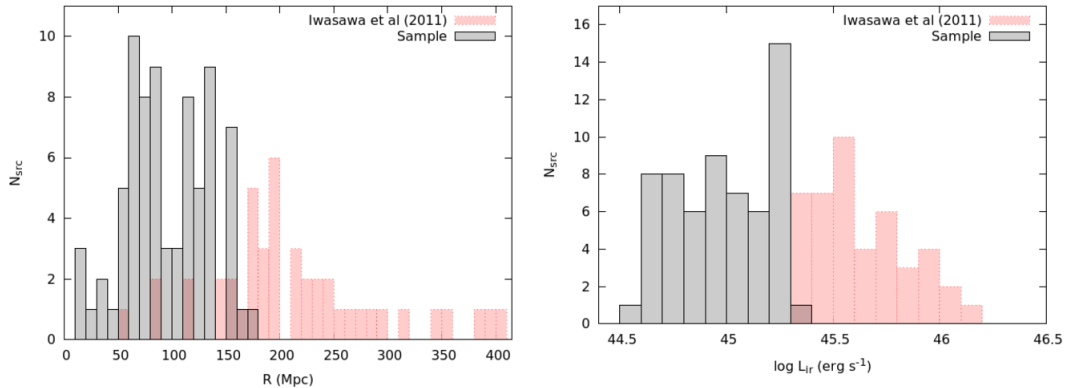


**Figure 5:** Luminosity distance (left) and infrared luminosity (right) distributions of the sample of study and the 44 system sample from Iwasawa *et al.*, (2011).

## 4.2 Observations and data reduction

Twenty-seven of the 59 objects were observed with Chandra in cycle-13 with a uniform 15 ks exposure on each target. All the observations were carried out in imaging mode with the ACIS-S detector operated in VFAINT mode. The Chandra data for the remaining 32 targets were taken from the Archive. The exposure times for these data go from 4.88 to 58.34 ks, all taken with ACIS-S in FAINT or VFAINT mode. When more than one observation was available, the one with longest exposure time was used. The observation log is shown in Table 2.

Galactic HI column density is estimated from the Leiden/Argentine/Bonn (LAB) survey (Kalberla *et al.*, 2005).

The data reduction was performed using the Chandra data analysis package CIAO version 4.7, and HEASARC’s FTOOLS.

Except for some sources, which are clearly absorbed AGN, Chandra spectra of the sources appears similar: an emission-line dominated soft X-ray band and a hard X-ray tail. Examples of both spectra can be seen in Fig. 6.

In order to estimate the X-ray fluxes for all sources, all components in multiple systems are analysed separately, as specified in Table 3. Fitting is done separately for the soft (0.5–2 keV) and hard (2–7 keV) X-ray components. Flux and luminosity in Table 3 are corrected only for galactic absorption, even if significant amount of intrinsic absorption may be present in the source. X-ray spectra of our objects is complex, and most of the spectra do not have sufficient quality to decompose and estimate intrinsic absorption for each component. For this reason, it is not corrected.

**Table 1:** The sample.

No.	IRAS Name	Optical ID	RA (NED) (J2000)	DEC (NED) (J2000)	z (km s <sup>-1</sup> )	D <sub>L</sub> (Mpc)	log(L <sub>ir</sub> ) (L <sub>⊙</sub> )
(1)	(2)	(3)	(4)	(5)	(6)	(7)	(8)
45	F13182+3424	UGC 08387	13 h20 m35.34 s	+34 d08 m22.2 s	0.023299	110.0	11.73
47	F01173+1405	CGCG 436-030	01 h20 m02.72 s	+14 d21 m42.9 s	0.031229	134.0	11.69
49	F01484+2220	NGC 0695	01 h51 m14.24 s	22 d34 m56.5 s	0.032472	139.0	11.69
50	F12592+0436	CGCG 043-099	13 h01 m50.80 s	+04 d20 m00.0 s	0.037483	175.0	11.68
51	F11011+4107	MCG+07-23-019	11 h03 m53.20 s	+40 d50 m57.0 s	0.034524	158.0	11.62
53	F02512+1446	UGC 02369	02 h54 m01.78 s	+14 d58 m24.9 s	0.031202	136.0	11.67
54	F04315-0840	NGC 1614	04 h33 m59.85 s	-08 d34 m44.0 s	0.015938	67.8	11.65
56	F13497+0220	NGC 5331	13 h52 m16.29 s	+02 d06 m17.0 s	0.033043	155.0	11.66
57	F06076-2139	IRAS F06076-2139	06 h09 m45.81 s	-21 d40 m23.7 s	0.037446	165.0	11.65
60	F11231+1456	IRAS F11231+1456	11 h25 m47.30 s	+14 d40 m21.1 s	0.034167	157.0	11.64
63	18090+0130	IRAS 18090+0130	18 h11 m35.91 s	+01 d31 m41.3 s	0.034167	134.0	11.65
64	F01417+1651	III Zw 035	01 h44 m30.45 s	+17 d06 m05.0 s	0.027436	119.0	11.64
65	F10257-4339	NGC 3256	10 h27 m51.27 s	-43 d54 m13.8 s	0.009354	38.9	11.64
67	F16399-0937	IRAS F16399-0937	16 h42 m40.21 s	-09 d43 m14.4 s	0.027012	128.0	11.63
68	F16164-0746	IRAS F16164-0746	16 h19 m11.79 s	-07 d54 m02.8 s	0.027152	128.0	11.62
71	F08354+2555	NGC 2623	08 h38 m24.08 s	+25 d45 m16.6 s	0.018509	84.1	11.60
72	F23135+2517	IC 5298	23 h16 m00.70 s	+25 d33 m24.1 s	0.027422	119.0	11.60
73	20351+2521	IRAS 20351+2521	20 h37 m17.72 s	+25 d31 m37.7 s	0.033697	151.0	11.61
75	F16104+5235	NGC 6090	16 h11 m40.70 s	+52 d27 m24.0 s	0.029304	137.0	11.58
79	F13362+4831	NGC 5256	13 h38 m17.52 s	+48 d16 m36.7 s	0.027863	129.0	11.56
80	F03359+1523	IRAS F03359+1523	03 h38 m46.70 s	+15 d32 m55.0 s	0.035401	152.0	11.55
81	F04210-4042	ESO 550-IG025	04 h21 m20.02 s	-18 d48 m47.6 s	0.032196	135.8	11.51
82	F00085-1223	NGC 0034	00 h11 m06.55 s	-12 d06 m26.3 s	0.019617	84.1	11.49
83	F00506+7248	MCG+12-02-001	00 h54 m03.61 s	+73 d05 m11.8 s	0.015698	69.8	11.50
85	F17138-1017	IRAS F17138-1017	17 h16 m35.79 s	-10 d20 m39.4 s	0.017335	84.0	11.49
95	F12043-3140	ESO 440-IG058	12 h06 m51.82 s	-31 d56 m53.1 s	0.023203	112.0	11.43
100	F21453-3511	NGC 7130	21 h48 m19.50 s	-34 d57 m04.7 s	0.016151	72.7	11.42
104	F23488+1949	NGC 7771	23 h51 m24.88 s	+20 d06 m42.6 s	0.014267	61.2	11.40
105	F23157-0441	NGC 7592	23 h18 m22.20 s	-04 d24 m57.6 s	0.024444	106.0	11.40
106	F16577+5900	NGC 6286	16 h58 m31.38 s	+58 d56 m10.5 s	0.018349	85.7	11.37
107	F12590+2934	NGC 4922	13 h01 m24.89 s	+29 d18 m40.0 s	0.023586	111.0	11.38
110	F10015-0614	NGC 3110	10 h04 m02.11 s	-06 d28 m29.2 s	0.016858	79.5	11.37
114	F00402-2349	NGC 0232	00 h42 m45.82 s	-23 d33 m40.9 s	0.022639	95.2	11.44
117	F09333+4841	MCG+08-18-013	09 h36 m37.19 s	+48 d28 m27.7 s	0.025941	117.0	11.34
120	F15107+0724	CGCG 049-057	15 h13 m13.09 s	+07 d13 m31.8 s	0.012999	65.4	11.35
121	F02401-0013	NGC 1068	02 h42 m40.71 s	-00 d00 m47.8 s	0.003793	15.9	11.40
123	F02435+1253	UGC 02238	02 h46 m17.49 s	+13 d05 m44.4 s	0.021883	92.4	11.33
127	F13197-1627	MCG-03-34-064	13 h22 m24.46 s	-16 d43 m42.9 s	0.016541	82.2	11.28
134	F00344-3349	ESO 350-IG038	00 h36 m52.25 s	-33 d33 m18.1 s	0.020598	89.0	11.28
136	F23394-0353	MCG -01-60-022	23 h42 m00.85 s	-03 d36 m54.6 s	0.023236	100.0	11.27
142	F13229-2934	NGC 5135	13 h25 m44.06 s	-29 d50 m01.2 s	0.013693	60.9	11.30
141	F13126+2453	IC 0860	13 h15 m03.53 s	+24 d37 m07.9 s	0.011164	56.8	11.14
147	F22132-3705	IC 5179	22 h16 m09.10 s	-36 d50 m37.4 s	0.011415	51.4	11.24
148	F03514+1546	CGCG 465-012	03 h54 m16.08 s	+15 d55 m43.4 s	0.022222	94.3	11.20
163	F12243-0036	NGC 4418	12 h26 m54.62 s	-00 d52 m39.2 s	0.007268	36.5	11.19
169	F21330-3846	ESO 343-IG013	21 h36 m10.83 s	-38 d32 m37.9 s	0.019060	85.8	11.14
170	F06107+7822	NGC 2146	06 h18 m37.71 s	+78 d21 m25.3 s	0.002979	17.5	11.12
174	F14280+3126	NGC 5653	14 h30 m10.42 s	+31 d12 m55.8 s	0.011881	60.2	11.13
178	F12116+5448	NGC 4194	12 h14 m09.47 s	+54 d31 m36.6 s	0.008342	43.0	11.10
179	F23157+0618	NGC 7591	23 h18 m16.28 s	+06 d35 m08.9 s	0.016531	71.4	11.12
182	F00073+2538	NGC 0023	00 h09 m53.41 s	+25 d55 m25.6 s	0.015231	65.2	11.12
188	F23133-4251	NGC 7552	23 h16 m10.77 s	-42 d35 m05.4 s	0.005365	23.5	11.11
191	F04118-3207	ESO 420-G013	04 h13 m49.69 s	-32 d00 m25.1 s	0.011908	51.0	11.07
194	08424-3130	ESO 432-IG006	08 h44 m28.07 s	-31 d41 m40.6 s	0.016165	74.4	11.08
195	F05365+6921	NGC 1961	05 h42 m04.65 s	+69 d22 m42.4 s	0.013122	59.0	11.06

**Table 1 – continued.**

No.	IRAS Name	Optical ID	RA (NED) (J2000)	DEC (NED) (J2000)	z (km s <sup>-1</sup> )	$D_L$ (Mpc)	$\log(L_{ir})$ ( $L_\odot$ )
(1)	(2)	(3)	(4)	(5)	(6)	(7)	(8)
196	F23444+2911	Arp 86	23 h47 m01.70 s	+29 d28 m16.3 s	0.016161	73.6	11.07
198	F03316-3618	NGC 1365	03 h33 m36.37 s	-36 d08 m25.4 s	0.005457	17.9	11.00
199	F10196+2149	NGC 3221	10 h22 m19.98 s	+21 d34 m10.5 s	0.013709	65.7	11.09
201	F02071-1023	NGC 0838	02 h09 m38.58 s	-10 d08 m46.3 s	0.012844	53.8	11.05

**Notes:** Column(1): through number of the object, also used in other tables. Column (2): original IRAS source, where an “F” prefix indicates the Faint Source Catalog and no prefix indicates the Point Source Catalog. Column (3): optical cross-identification, where available from NED. Column (4): the best available right ascension (J2000) in NED as of October 2008. Column (5): the best available source declination (J2000) from NED as of October 2008. Column (6): the best available heliocentric redshift from NED as of October 2008. Column (7): the luminosity distance in megaparsecs derived by correcting the heliocentric velocity for the 3-attractor flow model of Mould *et al.* (2000) and adopting cosmological parameters  $H_0 = 73 \text{ km s}^{-1} \text{ Mpc}^{-2}$ ,  $\Omega_V = 0.73$ , and  $\Omega_M = 0.27$ , as provided by NED. Column (8): the total infrared luminosity in  $\log_{10}$  Solar units computed using the flux densities reported in the RGBs and the luminosity distances in Col. (7) using the formulae  $L_{ir}/L_\odot = 4\pi(D_{L[m]})^2$ .

**Table 2:** Chandra observation log.

No.	Galaxy	Obs ID	Date	Mode	Exp. Time (ks)	0.5-7.0 keV <sup>a</sup> (cts)	$N_{H,Gal}^b$ ( $10^{20} \text{ cm}^{-2}$ )
45	UGC 08387	7811	2007-02-19	VFAINT	14.07	277.9 ± 17.1	1.0
47	CGCG 436-030	15047	2012-11-24	VFAINT	13.82	168.6 ± 13.8	3.4
49	NGC 0695	15046	2013-01-01	VFAINT	14.78	312.9 ± 18.5	6.9
50	CGCG 043-099	15048	2012-11-23	VFAINT	14.78	71.9 ± 8.1	1.9
51	MCG+07-23-019	12977	2011-02-07	VFAINT	52.34	506.9 ± 26.8	1.0
53	UGC 02369	4058	2002-12-14	FAINT	9.68	120.6 ± 12.0	7.9
54	NGC 1614	15050	2012-11-21	VFAINT	15.76	800.0 ± 28.9	6.3
56	NGC 5331	15051	2013-05-12	VFAINT	14.78	121.9 ± 12.4	2.0
57	IRAS F06076-2139	15052	2012-12-12	VFAINT	14.78	52.4 ± 8.2	7.6
60	IC 2810	15053	2013-10-27	VFAINT	14.78	93.2 ± 11.7	2.5
63	IRAS 18090+0130	15054	2013-02-10	VFAINT	14.77	98.9 ± 11.3	20.2
64	III Zw 035	6855	2006-02-24	FAINT	14.98	81.4 ± 9.0	4.8
65	NGC 3256	835	2000-01-05	FAINT	27.80	8117.2 ± 102.3	9.1
67	IRAS F16399-0937	15055	2013-06-30	VFAINT	14.87	161.9 ± 14.4	13.0
68	IRAS F16164-0746	15057	2013-01-19	VFAINT	14.78	99.2 ± 11.3	11.3
71	NGC 2623	4059	2003-01-03	FAINT	19.79	171.0 ± 14.1	3.1
72	IC 5298	15059	2013-02-04	VFAINT	14.78	222.8 ± 16.0	5.7
73	IRAS 20351+2521	15058	2012-12-13	VFAINT	13.56	146.8 ± 14.0	13.1
75	NGC 6090	6859	2006-05-14	FAINT	14.79	347.5 ± 19.3	1.6
79	NGC 5256	2044	2001-11-02	FAINT	19.69	1451.2 ± 43.5	1.7
80	IRAS F03359+1523	6856	2005-12-17	FAINT	14.76	108.2 ± 11.4	13.8
81	ESO 550-IG025	15060	2012-11-24	VFAINT	14.78	72.2 ± 10.6	3.2
82	NGC 0034	15061	2013-06-05	VFAINT	14.78	329.0 ± 19.5	2.1
83	MCG+12-02-001	15062	2012-11-22	VFAINT	14.31	311.0 ± 19.3	22.0
85	IRAS F17138-1017	15063	2013-07-12	VFAINT	14.78	207.3 ± 15.4	17.0
95	ESO 440-IG058	15064	2013-03-20	VFAINT	14.78	187.0 ± 16.1	5.6
100	NGC 7130	2188	2001-10-23	FAINT	38.64	3327.1 ± 59.3	1.9
104	NGC 7771	10397	2009-05-22	VFAINT	16.71	904.6 ± 34.6	4.0
105	NGC 7592	6860	2006-10-15	FAINT	14.99	388.7 ± 21.9	3.8
106	NGC 6286	10566	2009-09-18	FAINT	14.00	544.8 ± 27.9	1.8
107	NGC 4922	15065	2013-11-02	VFAINT	14.86	202.9 ± 17.2	0.9
110	NGC 3110	15069	2013-02-02	VFAINT	14.87	396.3 ± 22.3	3.5
114	NGC 0232	15066	2013-01-04	VFAINT	14.78	193.5 ± 15.7	1.4
117	MCG+08-18-013	15067	2013-06-03	VFAINT	13.79	101.7 ± 11.1	1.7

**Table 2 – continued.**

No.	Galaxy	Obs ID	Date	Mode	Exp. Time (ks)	0.5-7.0 keV <sup>a</sup> (cts)	$N_{H,Gal}^b$ ( $10^{20} \text{ cm}^{-2}$ )
120	CGCG 049-057	10399	2009-04-17	VFAINT	19.06	$30.2 \pm 7.6$	2.6
121	NGC 1068	344	2000-02-21	FAINT	47.44	$100828.1 \pm 326.7$	2.9
123	UGC 02238	15068	2012-12-02	VFAINT	14.87	$132.1 \pm 13.5$	8.9
127	MCG-03-34-064	7373	2006-07-31	FAINT	7.09	$1029.3 \pm 32.9$	5.0
134	ESO 350-IG038	8175	2006-10-28	VFAINT	54.00	$1794.5 \pm 45.8$	2.4
136	MCG -01-60-022	10570	2009-08-13	FAINT	18.90	$325.4 \pm 21.7$	3.6
142	NGC 5135	2187	2001-09-04	FAINT	29.30	$3975.9 \pm 68.0$	4.9
141	IC 0860	10400	2009-03-24	VFAINT	19.15	$25.9 \pm 7.2$	1.0
147	IC 5179	10392	2009-06-21	VFAINT	11.96	$555.5 \pm 32.2$	1.4
148	CGCG 465-012	15071	2012-12-17	VFAINT	14.87	$134.0 \pm 13.4$	14.8
163	NGC 4418	4060	2003-03-10	FAINT	19.81	$59.6 \pm 15.3$	1.9
169	ESO 343-IG013	15073	2013-06-13	VFAINT	14.78	$139.6 \pm 13.9$	2.8
170	NGC 2146	3135	2002-11-16	FAINT	10.02	$2144.2 \pm 50.4$	7.1
174	NGC 5653	10396	2009-04-11	VFAINT	16.52	$387.1 \pm 22.8$	1.3
178	NGC 4194	7071	2006-09-09	FAINT	35.50	$2410.3 \pm 51.4$	1.5
179	NGC 7591	10264	2009-07-05	FAINT	4.88	$26.3 \pm 6.1$	5.6
182	NGC 0023	10401	2008-10-27	VFAINT	19.45	$753.1 \pm 31.9$	3.4
188	NGC 7552	7848	2007-03-31	FAINT	5.08	$832.8 \pm 30.2$	1.2
191	ESO 420-G013	10393	2009-05-13	VFAINT	12.42	$759.0 \pm 29.2$	2.1
194	ESO 432-IG006	15074	2013-06-24	VFAINT	16.05	$280.7 \pm 20.0$	19.3
195	NGC 1961	10531	2009-05-08	VFAINT	32.83	$723.3 \pm 40.0$	8.1
196	NGC 7752/3	10569	2009-08-30	FAINT	11.99	$96.0 \pm 12.7$	5.4
198	NGC 1365	6869	2006-04-20	FAINT	15.54	$4644.2 \pm 72.7$	1.3
199	NGC 3221	10398	2009-03-19	VFAINT	19.03	$323.5 \pm 28.3$	1.9
201	NGC 0838	15667	2013-07-21	VFAINT	58.34	$1996.0 \pm 49.6$	2.6

**Notes:** <sup>(a)</sup> The source counts are corrected for background and measured in the 0.5–7.0 keV band. The counts from separate components in a single system are summed together. <sup>(b)</sup> The Galactic absorption column density is taken from the LAB HI map by Kalberla *et al.* (2005).

#### 4.2.1 Hard band fitting

In hard band, as emission is dominated either by an AGN component or by HMXB, explained in section 1.2, fitting is done with a powerlaw model. A correction for galactic absorption is added.

A powerlaw model gives  $dN/dE \propto E^{-\Gamma} \text{ cm}^{-2} \text{ s}^{-1} \text{ keV}^{-1}$ , with the photon index  $\Gamma$  related to the energy index  $\alpha$  ( $F_E \propto E^{-\alpha}$ ) as  $\Gamma = \alpha + 1$ . The photon index is determined for data with more than 30 cts in the energy range of interest.

In cases where the quality of the data does not allow for a good fit, the photon index is fixed at  $\Gamma = 2.0$  and only the normalization is left as a free parameter. In cases where the hard band spectra clearly corresponds to that of an absorbed AGN, intrinsic absorption is added to the powerlaw model, as a free parameter, and the photon index is fixed to  $\Gamma = 1.8$ . An example of such an absorbed AGN can be seen in Fig. 6.

#### 4.2.2 Soft band fitting

In the soft X-ray band, heavy blending of emission lines makes it difficult to distinguish between photoionized gas contribution from an AGN component and thermal

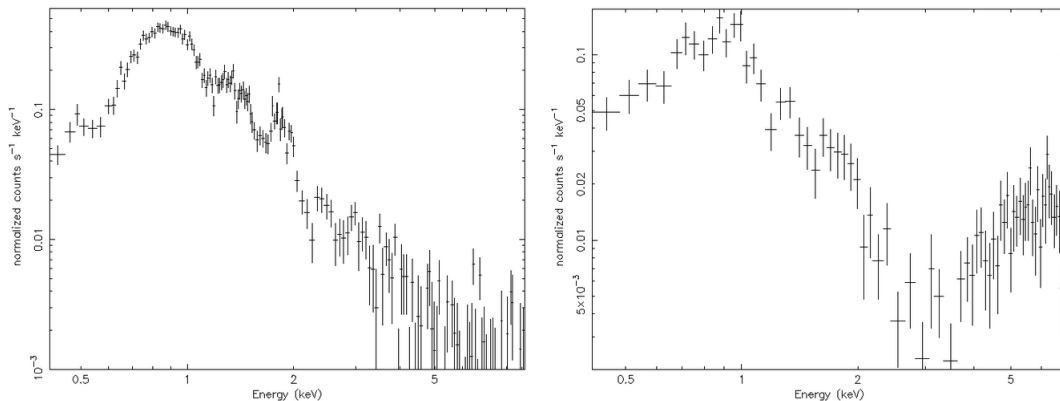


**Figure 6:** Chandra spectra of NGC 3256 (left), a typical starburst, and MCG-03-34-064 (right), an absorbed AGN. Both spectra are shown in the range 0.4 - 7 keV, including the hard and soft bands.

gas emission from a starburst.

However, it is generally assumed (Iwasawa *et al.*, 2011) that the dominating component in LIRGs is the thermal emission from hot plasma, arising from Bremsstrahlung electron interaction, even if for some objects there may be an important AGN contamination. A standard thermal emission spectrum model, with a solar abundance pattern, MEKAL (Mewe *et al.*, 1995), is used.

MEKAL model with only one component does not provide a good fit, even if corrected for galactic absorption, in all cases where the quality of data is good enough to compare with other options. In those cases, two MEKAL models, one with an associated lower temperature ( $\sim 1$  keV) and another with a higher temperature ( $\sim 1.5$  keV), are superposed.

The lower temperature component arises from a more extended plasma, easily absorbed in the inner regions of the galaxy (as its emission peaks in a softer band), resulting in an observed emission that is generated in the outer regions of the centre of the galaxy. Therefore, no intrinsic absorption from the source's gas is considered.

The higher temperature component produces an emission that peaks clearly in the centre of the nucleus, and even if it penetrates the surrounding material (as emission is harder), it is heavily absorbed by it. Therefore, this component has an intrinsic absorption added as a free parameter.

### 4.2.3 Special cases

For a few specific galaxies the hard and soft band fitting described above produced unsatisfactory results, and a single model for all the spectra (0.5–7 keV) resulted in a better adjustment. It is the case of MCG+12-02-001 (W), CGCG 049-057, NGC 4418, ESO 343-IG013 (N) and ESO 343-IG013 (S), for which a powerlaw was used to described the whole X-ray range (0.5–7 keV); and for ESO 440-IG058 (N), for which a one component MEKAL model was used for the whole range.

### 4.3 Results

Results of the data analysis of Chandra spectra are presented in Table 3. For each galaxy, count rates in soft and hard band, X-ray colour, estimated X-ray fluxes and luminosities in the two bands, and the logarithmic ratio to the infrared luminosity in the  $8 - 1000 \mu\text{m}$  (as obtained from Armus *et al.*, 2009), are listed.

Count rates are computed for each component inside a system separately, as opposed to the source counts in Table 2, as well as with flux and luminosity in each band. IR luminosity is divided into the respective components with a ratio estimated from Spitzer MIPS photometry, with the exception of the three systems marked in Table 3, as they appeared as unresolved sources. The X-ray colour is defined as  $HR = (H - S)/(H + S)$ , also referred to as ‘‘Hardness Ratio’’, where  $H$  and  $S$  are background corrected counts in the 2–8 keV and in the 0.5–2 keV bands respectively.

#### 4.3.1 AGN selection

The hardness ratio gives the relative strength of the X-ray emission above and below 2 keV, in counts. Emission above 2 keV being much stronger, implying a higher  $HR$ , is often associated with an absorbed X-ray source, which indicates the presence of an obscured AGN. As described in Iwasawa *et al.* (2009), AGN can be selected by the hardness of the X-ray emission, classifying objects with  $HR > -0.3$  as AGN. This threshold is chosen because ULIRGs known to host AGN cluster just above this value. This method may miss some Compton-thick AGN, as they are also absorbed in the hard band and only reflected radiation is observed.

The values of  $HR$  as a function of  $L_X$  are plotted in Fig. 7, the median of the distribution is -0.59.

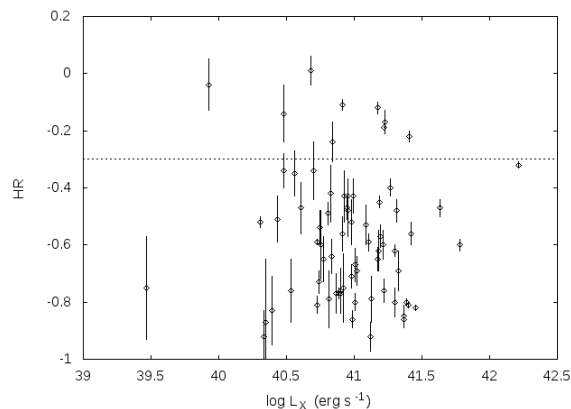


**Figure 7:** Hardness ratio as a function of X-ray luminosity, derived for single components in every system (see Table 3.). The threshold for selecting AGN,  $HR > -0.3$ , is shown with a dashed line. The median is -0.59.

Selection of AGN can also be carried out using infrared observations. For the

**Table 3:** X-ray spectral properties for the sample.

No.	Galaxy	$SX$ (1)	$HX$ (2)	$HR$ (3)	$F_{SX}$ (4)	$F_{HX}$ (5)	$L_{SX}$ (6)	$L_{HX}$ (7)	$SX/IR$ (8)	$HX/IR$ (9)
45	UGC 08387	15.47 ± 1.06	4.28 ± 0.59	-0.57 ± 0.04	5.18	5.57	7.50	8.07	-4.44	-4.41
47	CGCG 436-030	9.01 ± 0.84	3.18 ± 0.54	-0.48 ± 0.04	4.07	5.50	8.75	11.83	-4.33	-4.20
49	NGC 0695	15.58 ± 1.06	5.59 ± 0.66	-0.47 ± 0.03	6.83	11.68	15.78	27.01	-4.08	-3.84
50	CGCG 043-099	2.60 ± 0.44	0.92 ± 0.32	-0.48 ± 0.09	1.09	1.35	3.98	4.96	-4.67	-4.57
51	MCG+07-23-019	8.51 ± 0.45	1.17 ± 0.24	-0.76 ± 0.04	3.65	1.93	10.91	5.76	-4.17	-4.44
53	UGC 02369 (S)	11.16 ± 1.14	1.30 ± 0.48	-0.79 ± 0.08	4.31	1.72	9.53	3.81	-4.28	-4.67
54	NGC 1614	38.57 ± 1.59	12.19 ± 0.91	-0.52 ± 0.02	1.82	1.87	1.00	1.03	-5.23	-5.22
56	NGC 5331 (N)	1.79 ± 0.38	0.73 ± 0.26	-0.42 ± 0.10	1.01	1.32	2.89	3.79	-4.18	-4.06
56	NGC 5331 (S)	4.37 ± 0.59	1.36 ± 0.36	-0.53 ± 0.07	2.25	1.97	6.46	5.68	-4.31	-4.37
57	IRAS F06076-2139(N)	2.54 ± 0.44	1.00 ± 0.33	-0.43 ± 0.09	1.37	1.23	4.45	4.01	-4.59	-4.63
60	IC 2810(NW)	3.88 ± 0.57	0.55 ± 0.35	-0.75 ± 0.12	1.88	0.96	5.53	2.83	-(a)	-(a)
60	IC 2810 (SE)	1.75 ± 0.39	0.12 ± 0.19	-0.87 ± 0.22	0.75	0.01	2.20	0.02	-(a)	-(a)
63	IRAS 18090+0130 (E)	4.01 ± 0.55	1.27 ± 0.36	-0.52 ± 0.08	1.90	2.58	4.08	5.54	-4.62	-4.49
63	IRAS 18090+0130(W)	1.08 ± 0.30	0.33 ± 0.23	-0.54 ± 0.18	-(b)	-(b)	-(b)	-(b)	-(b)	-(b)
64	III Zw 035 (N)	2.34 ± 0.41	0.84 ± 0.26	-0.47 ± 0.09	1.07	1.33	1.81	2.25	-4.97	-4.87
64	III Zw 035 (S)	0.96 ± 0.27	0.73 ± 0.24	-0.14 ± 0.10	0.39	1.39	0.66	2.35	-(c)	-(c)
65	NGC 3256	263.36 ± 3.28	28.62 ± 1.67	-0.80 ± 0.01	89.99	43.60	16.29	7.89	-4.01	-4.33
67	IRAS F16399-0937(N)	4.02 ± 0.53	1.60 ± 0.34	-0.43 ± 0.06	2.06	2.56	4.03	5.02	-(a)	-(a)
67	IRAS F16399-0937(S)	2.06 ± 0.38	1.25 ± 0.31	-0.24 ± 0.07	1.42	2.10	2.79	4.12	-(a)	-(a)
68	IRAS F16164-0746	3.91 ± 0.55	2.80 ± 0.52	-0.17 ± 0.04	1.90	6.72	3.73	13.17	-4.63	-4.09
71	NGC 2623	4.79 ± 0.52	3.85 ± 0.49	-0.11 ± 0.02	1.76	7.95	1.49	6.72	-5.01	-4.36
72	IC 5298	11.76 ± 0.92	3.31 ± 0.56	-0.56 ± 0.04	5.92	9.66	10.03	16.36	-4.18	-3.97
73	IRAS 20351+2521	9.14 ± 0.89	1.69 ± 0.52	-0.69 ± 0.07	5.14	2.60	14.02	7.09	-4.05	-4.34
75	NGC 6090 (NE)	16.71 ± 1.07	1.84 ± 0.37	-0.80 ± 0.05	6.07	2.88	13.63	6.47	-(a)	-(a)
75	NGC6090 (SW)	4.68 ± 0.57	0.56 ± 0.21	-0.79 ± 0.10	1.78	1.13	4.00	2.53	-(a)	-(a)
79	NGC 5256 (NE)	32.39 ± 1.31	7.97 ± 0.69	-0.60 ± 0.02	12.17	18.06	24.23	35.95	-3.28	-3.11
79	NGC 5256 (SW)	20.47 ± 1.02	1.70 ± 0.32	-0.85 ± 0.04	8.32	3.31	16.56	6.58	-3.75	-4.15
80	IRAS F03359+1523(E)	5.92 ± 0.67	1.41 ± 0.38	-0.62 ± 0.07	3.14	2.34	8.68	6.48	-4.20	-4.32
81	ESO 550-IG025 (N)	2.23 ± 0.41	0.55 ± 0.24	-0.60 ± 0.12	1.03	1.55	2.27	3.42	-4.44	-4.26
81	ESO 550-IG025 (S)	1.55 ± 0.35	0.76 ± 0.26	-0.34 ± 0.10	0.75	1.51	1.65	3.34	-4.58	-4.27
82	NGC 0034	15.58 ± 1.08	6.68 ± 0.76	-0.40 ± 0.03	7.56	14.26	6.40	12.07	-4.27	-3.99
83	MCG+12-02-001 (E)	11.12 ± 0.89	3.77 ± 0.53	-0.49 ± 0.04	5.16	5.77	3.01	3.37	-4.56	-4.51
83	MCG+12-02-001 (W)	3.02 ± 0.46	1.49 ± 0.34	-0.34 ± 0.06	2.16	2.99	1.26	1.75	-(c)	-(c)
85	IRAS F17138-1017	7.84 ± 0.76	6.19 ± 0.71	-0.12 ± 0.02	4.67	12.87	3.94	10.86	-4.48	-4.04
95	ESO 440-IG058 (N)	2.12 ± 0.38	1.02 ± 0.27	-0.35 ± 0.08	1.15	1.28	1.72	1.92	-(c)	-(c)
95	ESO 440-IG058 (S)	7.16 ± 0.70	0.97 ± 0.28	-0.76 ± 0.08	3.73	1.54	5.60	2.31	-4.23	-4.61
100	NGC 7130	78.11 ± 1.44	8.00 ± 0.53	-0.81 ± 0.01	26.71	13.31	16.89	8.42	-3.78	-4.08
104	NGC 7771	33.16 ± 1.54	12.55 ± 1.14	-0.45 ± 0.02	13.96	20.28	6.26	9.09	-4.09	-3.93
104	NGC 7770 (NGC7771S)	8.08 ± 0.73	0.34 ± 0.29	-0.92 ± 0.09	3.55	1.28	1.59	0.57	-4.08	-4.53
105	NGC 7592 (E)	8.42 ± 0.76	1.11 ± 0.32	-0.77 ± 0.07	3.68	1.81	4.94	2.43	-4.09	-4.40
105	NGC 7592 (W)	11.29 ± 0.88	2.04 ± 0.41	-0.69 ± 0.05	4.63	3.17	6.23	4.26	-3.75	-3.92
106	NGC 6286	32.15 ± 1.64	1.27 ± 0.87	-0.92 ± 0.05	12.44	2.58	10.93	2.27	-3.79	-4.47
106	NGC 6285 (NGC 6286 NW)	5.04 ± 0.64	0.45 ± 0.33	-0.83 ± 0.12	1.97	0.86	1.73	0.75	-4.11	-4.48
107	NGC 4922	10.93 ± 0.97	2.73 ± 0.62	-0.60 ± 0.05	5.08	5.93	7.49	8.74	-4.09	-4.02
110	NGC 3110	21.92 ± 1.28	4.73 ± 0.77	-0.65 ± 0.04	11.30	8.43	8.54	6.37	-4.02	-4.15
114	NGC 0232	10.91 ± 0.91	2.19 ± 0.55	-0.67 ± 0.06	4.95	4.35	5.37	4.72	-4.29	-4.35
117	MCG+08-18-013(E)	5.27 ± 0.67	2.1 ± 0.45	-0.43 ± 0.06	2.49	3.57	4.07	5.85	-4.32	-4.16
120	CGCG 049-057	0.83 ± 0.28	0.76 ± 0.29	-0.04 ± 0.09	0.40	1.26	0.20	0.64	-5.63	-5.13
121	NGC 1068	1975.11 ± 6.58	150.27 ± 2.03	-0.86 ± 0.00	539.24	224.33	16.31	6.79	-3.77	-4.15
123	UGC 02238	6.94 ± 0.74	1.94 ± 0.52	-0.56 ± 0.06	3.70	4.38	3.77	4.47	-4.34	-4.26
127	MCG-03-34-064	95.67 ± 3.73	49.50 ± 2.75	-0.32 ± 0.01	43.43	158.12	35.11	127.83	-3.32	-2.76
134	ESO 350-IG038	26.85 ± 0.73	6.38 ± 0.43	-0.62 ± 0.02	10.91	10.06	10.34	9.53	-3.85	-3.89
136	MCG -01-60-022	10.52 ± 0.84	6.70 ± 0.78	-0.22 ± 0.02	4.53	16.82	5.42	20.13	-4.12	-3.55
142	NGC 5135	123.31 ± 2.14	12.39 ± 0.90	-0.82 ± 0.01	44.38	19.85	19.69	8.81	-3.59	-3.94

**Table 3 – continued.**

No.	Galaxy	$SX$ (1)	$HX$ (2)	$HR$ (3)	$F_{SX}$ (4)	$F_{HX}$ (5)	$L_{SX}$ (6)	$L_{HX}$ (7)	$SX/IR$ (8)	$HX/IR$ (9)
141	IC 0860	$0.68 \pm 0.26$	$0.37 \pm 0.27$	$-0.29 \pm 0.17$	– <sup>(b)</sup>					
147	IC 5179	$39.74 \pm 2.14$	$6.71 \pm 1.62$	$-0.71 \pm 0.04$	15.79	14.40	4.99	4.55	-4.13	-4.17
148	CGCG 465–012	$7.13 \pm 0.77$	$1.52 \pm 0.58$	$-0.65 \pm 0.08$	3.10	2.46	3.29	2.62	-4.27	-4.37
163	NGC 4418	$2.63 \pm 0.59$	$0.38 \pm 0.32$	$-0.75 \pm 0.18$	0.92	0.91	0.15	0.15	-5.61	-5.61
169	ESO 343–IG013 (N)	$2.02 \pm 0.38$	$2.05 \pm 0.38$	$0.01 \pm 0.05$	0.96	4.46	0.85	3.93	-4.72	-4.05
169	ESO 343–IG013 (S)	$3.15 \pm 0.47$	$1.02 \pm 0.30$	$-0.51 \pm 0.08$	1.84	1.24	1.62	1.10	– <sup>(c)</sup>	– <sup>(c)</sup>
170	NGC 2146	$170.25 \pm 4.38$	$43.74 \pm 2.47$	$-0.59 \pm 0.01$	68.25	76.39	2.50	2.80	-4.31	-4.26
174	NGC 5653	$20.26 \pm 1.20$	$3.18 \pm 0.70$	$-0.73 \pm 0.04$	8.29	4.44	3.59	1.93	-4.16	-4.43
178	NGC 4194	$59.99 \pm 1.33$	$7.91 \pm 0.57$	$-0.77 \pm 0.02$	23.62	12.43	5.23	2.75	-3.97	-4.25
179	NGC 7591	$4.29 \pm 1.01$	$1.09 \pm 0.74$	$-0.59 \pm 0.17$	– <sup>(b)</sup>					
182	NGC 0023	$34.84 \pm 1.45$	$3.88 \pm 0.77$	$-0.80 \pm 0.03$	13.99	6.07	7.12	3.09	-3.85	-4.22
188	NGC 7552	$148.31 \pm 5.56$	$15.63 \pm 2.09$	$-0.81 \pm 0.03$	56.93	24.29	3.76	1.60	-4.12	-4.49
191	ESO 420–G013	$56.94 \pm 2.19$	$4.17 \pm 0.83$	$-0.86 \pm 0.03$	25.27	5.83	7.86	1.81	-3.76	-4.40
194	ESO 432–IG006 (NE)	$8.09 \pm 0.76$	$1.75 \pm 0.48$	$-0.64 \pm 0.06$	5.76	4.46	3.82	2.96	-3.78	-3.89
194	ESO 432–IG006 (SW)	$6.04 \pm 0.66$	$1.81 \pm 0.46$	$-0.54 \pm 0.06$	4.33	4.03	2.87	2.67	-3.91	-3.94
195	NGC 1961	$17.55 \pm 0.89$	$4.48 \pm 0.83$	$-0.59 \pm 0.03$	14.94	15.77	6.22	6.57	-3.85	-3.83
196	NGC 7752/3	$7.05 \pm 0.85$	$0.96 \pm 0.62$	$-0.76 \pm 0.11$	3.02	2.24	1.96	1.45	-4.36	-4.49
198	NGC 1365	$177.35 \pm 3.63$	$121.5 \pm 2.95$	$-0.19 \pm 0.00$	68.22	364.21	2.62	13.96	-4.17	-3.44
199	NGC 3221	$12.47 \pm 1.08$	$4.53 \pm 1.02$	$-0.47 \pm 0.04$	5.01	12.22	2.59	6.31	-4.26	-3.88
201	NGC 0838	$30.31 \pm 0.75$	$3.91 \pm 0.39$	$-0.77 \pm 0.02$	15.87	6.53	5.50	2.26	-3.89	-4.28

**Notes:** Column (1): background corrected count rate in the 0.5–2 keV band in units of  $10^{-3}$  ct s $^{-1}$ . Column (2): background corrected count rate in the 2–7 keV band in units of  $10^{-3}$  ct s $^{-1}$ . Column (3): X-ray colour as defined by  $HR = (H - S)/(H + S)$ . Column (4): observed 0.5–2 keV band flux corrected for Galactic absorption in units of  $10^{14}$  erg s $^{-1}$  cm $^{-2}$ . Column (5): observed 2–7 keV band flux corrected for Galactic absorption in units of  $10^{14}$  erg s $^{-1}$  cm $^{-2}$ . Column (6): 0.5–2 keV band luminosity corrected for Galactic absorption in units of  $10^{40}$  erg s $^{-1}$ . Column (7): 2–7 keV band luminosity corrected for Galactic absorption in units of  $10^{40}$  erg s $^{-1}$ . Column (8): logarithmic luminosity ratio of the 0.5–2 keV and 8–1000  $\mu$ m bands. Column (9): logarithmic luminosity ratio of the 2–8 keV and 8–1000  $\mu$ m bands. <sup>(a)</sup> Missing values due to inability to separate IRAS IR flux into two components (unresolved sources in MIPS 24). <sup>(b)</sup> Missing values due to inability to fit X-ray spectra, not enough source counts. <sup>(c)</sup> Missing values due to all IRAS IR flux in the system being originated in the source’s companion.

GOALS sample two main approaches have been followed: detection of the [Ne V] 14.3  $\mu$ m line over kpc scales, which provides direct evidence for the presence of an AGN (Petric *et al.*, 2011), and the equivalent width of the 6.2  $\mu$ m PAH feature being lower than 0.1  $\mu$ m (Stierwalt *et al.*, 2013). From the data presented in the two mentioned papers and the X-ray  $HR$  selection from this work’s study, which are complementary, a list of AGN within this work’s sample is presented in Table 4. A total of 24 galaxies fit into at least one of the three criteria (a 32 % of our sample).

#### 4.3.2 X-ray luminosities and correlation with IR

The distribution of X-ray luminosities, compared to the Iwasawa *et al.* (2011) sample, is shown in Fig. 8. It has a median logarithmic value of  $\log(L_X) \sim 41.1$  erg s $^{-1}$ . Iwasawa *et al.* sample has a median of  $\log(L_X) \sim 41.6$  erg s $^{-1}$ , but a wider distribution. A weak correlation between IR and X-ray luminosity can be seen in Fig. 9, with a typical spread of over one order of magnitude. When multiple components are present in a system they are represented separately, except for the cases

**Table 4:** AGN selection according to any of the three mentioned methods in section 4.3.1.

No.	Galaxy	[Ne v] 14.3 $\mu\text{m}$	6.2 $\mu\text{m}$ EQW( $\sigma$ ) ( $\mu\text{m}$ )	$HR$
		(1)	(2)	(3)
45	UGC 08387	Y	0.62 (0.01)	$-0.57 \pm 0.04$
64	III Zw 035 (S)	N	— <sup>(a)</sup>	$-0.14 \pm 0.10$
67	IRAS F16399-0937(S)	N	0.43 (0.01)	$-0.24 \pm 0.07$
68	IRAS 16164-0746	Y	0.61 (0.01)	$-0.17 \pm 0.04$
71	NGC 2623	Y	0.27 (0.01)	$-0.11 \pm 0.02$
72	IC 5298	Y	0.12 (0.004)	$-0.56 \pm 0.04$
79	NGC 5256 (NE)	Y	0.44 (0.02) <sup>(b)</sup>	$-0.60 \pm 0.02$
79	NGC 5256 (SW)	Y	0.44 (0.02) <sup>(b)</sup>	$-0.85 \pm 0.04$
85	IRAS F17138-1017	N	0.68 (0.01)	$-0.12 \pm 0.02$
100	NGC 7130	Y	0.30 (0.01)	$-0.81 \pm 0.01$
105	NGC 7592 (E)	Y <sup>(b)</sup>	0.48 (0.01)	$-0.77 \pm 0.07$
105	NGC 7592 (W)	Y <sup>(b)</sup>	0.30 (0.01)	$-0.69 \pm 0.05$
107	NGC 4922	Y	0.16 (0.003)	$-0.60 \pm 0.05$
114	NGC 0232	Y	0.16 (0.005)	$-0.67 \pm 0.06$
120	CGCG 049-057	N	0.51 (0.04)	$-0.04 \pm 0.09$
121	NGC 1068	Y	— <sup>(c)</sup>	$-0.86 \pm 0.00$
127	MCG -03-34-064	Y	$<0.01$ (—)	$-0.32 \pm 0.01$
136	MCG -01-60-022	N	— <sup>(a)</sup>	$-0.22 \pm 0.02$
141	IC 0860	N	0.43 (0.01)	$-0.29 \pm 0.17$
142	NGC 5135	Y	0.49 (0.01)	$-0.82 \pm 0.01$
163	NGC 4418	N	$<0.02$ (—)	$-0.75 \pm 0.18$
169	ESO 343-IG013 (N)	N	0.47 (0.01)	$0.01 \pm 0.05$
191	ESO 420-G013	Y	0.30 (0.003)	$-0.86 \pm 0.03$
198	NGC 1365	N	0.13 (0.002)	$-0.19 \pm 0.00$

**Notes:** (1) Detection of the [Ne v] 14.3  $\mu\text{m}$  line over kpc scales in Petric *et al* (2011) observations. (2) Equivalent width of the 6.2  $\mu\text{m}$  PAH feature in Stierwalt *et al.* (2013). (3) Hardness ratio as calculated with this work’s data. All galaxies of this work’s sample that are selected by any of the three criteria described are listed. <sup>(a)</sup>Not analysed galaxies due to archival SL staring mode observations not centred on the galaxy’s nucleus. <sup>(b)</sup>Galaxies not resolved in MIR observations in any of the two mentioned papers. <sup>(c)</sup>Galaxy observation saturated the spectrograph, not analysed.

where IR sources were not resolved (shown in Table 3), being then plotted with the system’s overall luminosity.

The data shows a significant spread, caused by the scatter around the linear correlation, rather than any non-linear one. The adjusted correlation has slope 1 in the logarithmic plane, for better comparison with results from previous works.

Adjustment is  $\log(L_{SX}) = \log(L_{ir}) - 4.22 \pm 0.44$  for the soft X-rays and  $\log(L_{HX}) = \log(L_{ir}) - 4.24 \pm 0.42$  for the hard X-rays, where the uncertainties are the dispersion of the distribution. Correlation coefficients for the two distributions are, respectively, 0.24 and 0.37.

Values obtained by Iwasawa *et al.* in their higher IR luminosity GOALS sub-sample are  $\log(L_{SX}) = \log(L_{ir}) - 4.53 \pm 0.34$  and  $\log(L_{HX}) = \log(L_{ir}) - 4.40 \pm 0.63$ .

Removing sources indicated as AGN in Table 4 from our sample results in obtaining  $\log(L_{SX}) = \log(L_{ir}) - 4.21 \pm 0.28$  for the soft band and  $\log(L_{HX}) = \log(L_{ir}) - 4.29 \pm 0.30$  for the hard band. Correlation coefficients then become 0.26 and 0.46, respectively. Comparison between the obtained results at high star formation rates for this work’s sample and Iwasawa *et al.* (2011) sample are shown

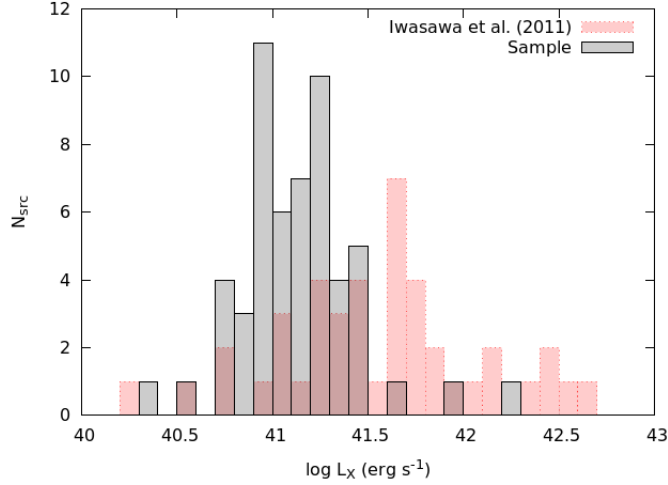


**Figure 8:** Derived total X-ray luminosity distribution of the sample of study (as in Table 3) and the 44 system sample from Iwasawa *et al.*, (2011).

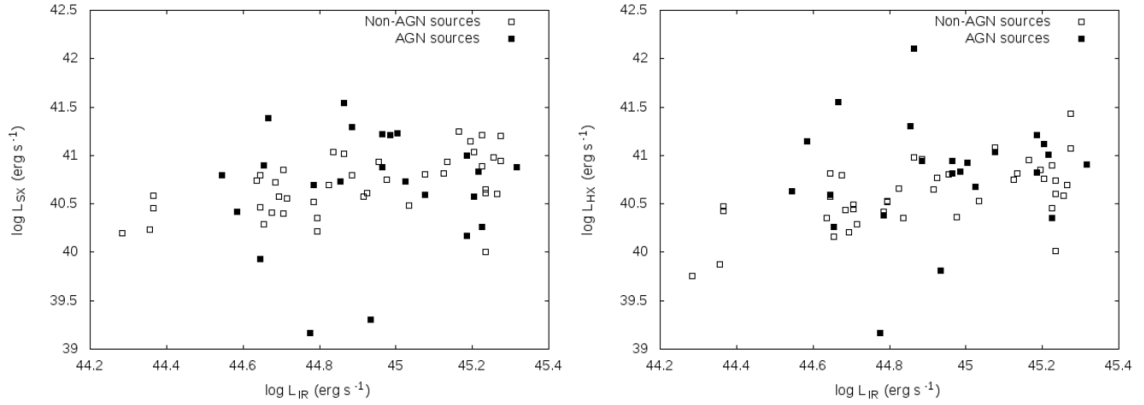


**Figure 9:** Plots of X-ray (left: soft band, right: hard band) versus infrared luminosity. AGN from Table 4 are marked in black.

in Fig. 10.

For local, star-forming galaxies with lower star formation rates ( $3 - 30 M_{\odot} \text{ yr}^{-1}$ ), obtained correlations give significantly larger values for the logarithmic quotient e.g.  $\log(L_{SX}) = \log(L_{ir}) - 3.70$  for soft band and  $\log(L_{SX}) = \log(L_{ir}) - 3.68$  for hard band (Ranalli *et al.*, 2003 [R03]).

However, a direct comparison with the Ranalli *et al.* (2003) results would require a correction for different infrared band-passes (Iwasawa *et al.*, 2009), which consists in calculating the far infrared luminosity as:

$$FIR = 1.26 \cdot 10^{11} (2.58 S_{60\mu} + S_{100\mu}) \text{ erg s}^{-1} \text{ cm}^{-2} \quad (1)$$

where  $S_{60\mu}$  and  $S_{100\mu}$  are infrared fluxes in Jy, taken from the IRAS Faint Source Catalog. Infrared luminosity for our sample is recalculated using (1), and compared

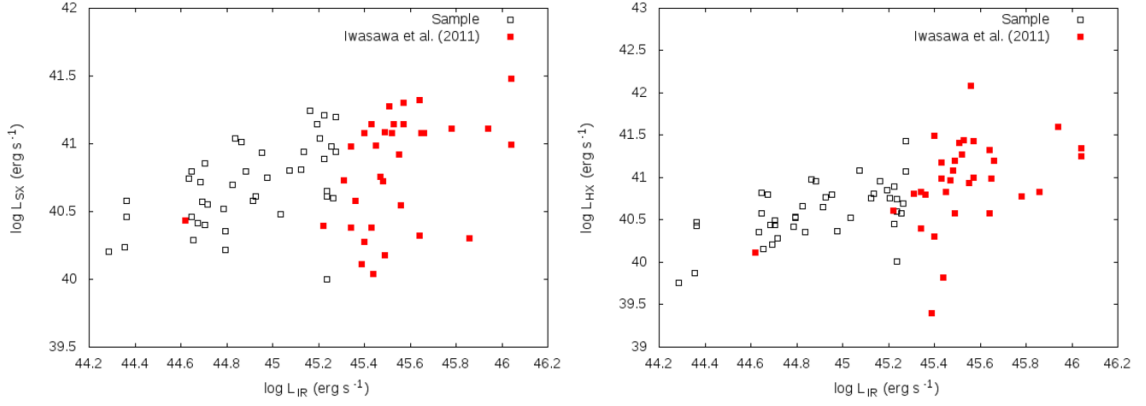


**Figure 10:** Plots of X-ray (left: soft band, right: hard band) versus infrared luminosity. Iwasawa *et al.* (2011) results are shown in red. All AGN sources are removed from both samples.

to the R03 correlation, as shown in Fig. 11.

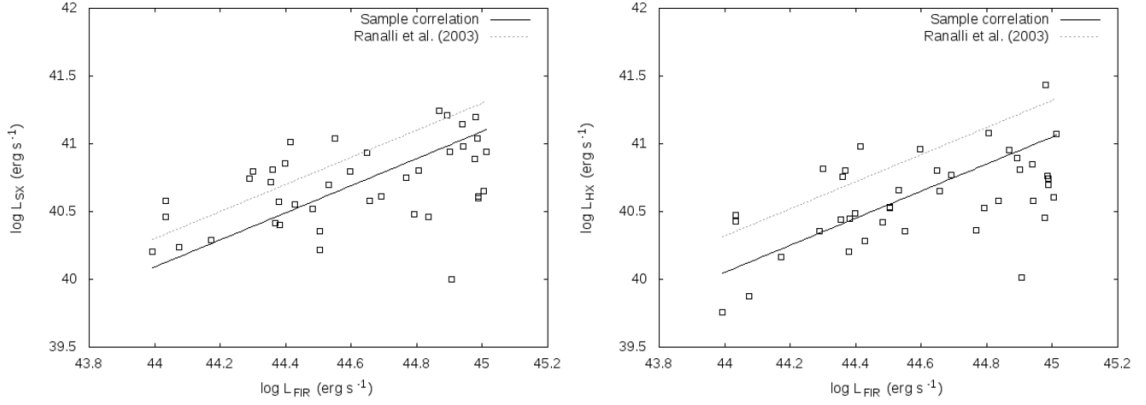


**Figure 11:** Plots of X-ray (left: soft band, right: hard band) versus far infrared luminosity for this work's sample, recalculated with expression (1). Extrapolation of the Ranalli *et al.* (2003) correlation, derived for local, low star formation rate galaxies is shown as a dashed line.

Again, a weak correlation is obtained, with a significant spread:  $\log(L_{SX}) = \log(L_{ir}) - 3.91 \pm 0.31$  for the soft X-rays and  $\log(L_{HX}) = \log(L_{ir}) - 3.95 \pm 0.30$  for the hard X-rays, where the uncertainties are the dispersion of the distribution. Correlation coefficients for soft and hard band fluxes and far infrared flux are, respectively, 0.47 and 0.54.

As can be qualitatively seen in Fig. 11, most of this work's sample is below the extrapolation of the R03 correlation to higher luminosities.

## 5 Discussion

### 5.1 X-ray and infrared luminosity correlation

In this work, the correlation between the infrared (in the 8–1000  $\mu\text{m}$  band) and X-ray luminosity, in soft and in hard band, in a sample of 59 GOALS systems, containing 74 individual galaxies, has been studied. As seen in Fig. 9, a weak correlation is obtained:  $\log(L_{SX}) = \log(L_{ir}) - 4.22 \pm 0.19$  for the soft X-rays and  $\log(L_{HX}) = \log(L_{ir}) - 4.24 \pm 0.18$  for the hard X-rays.

The assumption that X-ray luminosity could trace the SFR in galaxies is based on the correlation, initially found in nearby star-forming galaxies with SFRs  $\sim 3 - 30 M_{\odot} \text{ yr}^{-1}$  (e.g. Ranalli *et al.*, 2003; Grimm *et al.*, 2003; Mineo *et al.*, 2014), as  $\log(L_X) \sim \log(L_{ir}) - 3.7$ . This relation appears to extend to objects with higher SFR, up to  $\sim 100 M_{\odot} \text{ yr}^{-1}$ , and higher redshifts (e.g. Hornschemeier *et al.*, 2005; Persic and Rephaeli, 2007; Lehmer *et al.*, 2008).

The hard X-ray emission is assumed to come mainly from high mass X-ray binaries, which are expected to have a close relationship with the starburst, and therefore the correlation holds.

However, there are indications that objects with a very high SFR (up to  $\sim 1000 M_{\odot} \text{ yr}^{-1}$ ), such as ULIRGs, might depart from the correlation due to being underluminous in X-rays (e.g. Persic and Rephaeli, 2007; Barger *et al.*, 2007). The same conclusion seems to be reached by Iwasawa *et al.* (2011) and this work's results.

In a direct comparison with the R03 correlation, obtaining the infrared luminosity from expression (1), the correlation between infrared and X-ray luminosity is still weak and presents dispersion over one order of magnitude. The difference between R03 correlation and the one derived for our sample is of  $\sim 0.2$  dex. This can be appreciated in Fig. 11, specially for the hard X-ray band luminosities. These results suggest the previous claim that star formation rate can be directly inferred from X-ray luminosity may not hold for dusty galaxies like LIRGs.

A possible explanation comes from the results of the study of the X-ray spectra of Arp 220 (Iwasawa *et al.*, 2005). For this galaxy, the  $\log(L_X/L_{ir})$  is  $\sim 1$  dex below the general  $L_X - L_{ir}$  correlation at low SFRs, and its spectra presents a high ionization Fe K line (mainly Fe XXV), which implies that the X-ray emission is not dominated by X-ray binaries, because of the spectral incompatibility.

To explain why the X-ray binaries are not dominant in X-rays and the departure from the correlation, there are two possibilities: either the High-mass X-ray binaries are obscured from view, or the infrared and X-ray luminosity comes from a different source, possibly unrelated to the star formation processes.

Assuming obscuration of binaries is the cause, a column density of  $N_H \sim 10^{25} \text{ cm}^{-2}$  would be needed. A dense, nuclear molecular disk ( $\sim 10^9 M_{\odot}$ ) is often found in the central part of ULIRGs (e.g. Medling *et al.*, 2014), therefore such a high column density is possible. Then, the high ionization Fe K line can be explained by high temperature thermal gas ( $T \sim 10^8 \text{ K}$ ) produced by the starburst. For Arp 220

(Iwasawa *et al.*, 2005) the observed features in the spectra can be reproduced with these assumptions.

Assuming emission does not come from HMXB, with the presence of the mentioned nuclear molecular disks, a heavily obscured AGN would also be a possibility. X-ray light would have difficulty escaping from the inner regions, but the high-ionization line could then originate from extended, low density gas photoionized by the AGN. This has been observed in Compton thick AGN (e.g. NGC 1068).

In Arp 220 measurements, the observation of a steep temperature gradient in the western nucleus provides argument for the existence of an AGN (Downes and Eckart, 2007), and millimetre molecular line observations also suggest an X-ray-dominated chemistry, which again favours heating by an AGN (Aalto, 2008; Imanishi *et al.*, 2007).

The same explanation may be valid for sources in the GOALS sample, since all of them are (U)LIRGs, making it likely for them to contain an AGN, activated due to mergers or interaction as described in section 1.1.2, heavily obscured by the large amounts of molecular gas and dust characteristic of this type of galaxies. The AGN may be responsible for the powering of a significant fraction of the infrared luminosity, while having its X-ray output absorbed by its surrounding material, thus appearing underluminous in X-rays when compared with the Ranalli *et al.* (2003) correlation.

Furthermore, in the Iwasawa *et al.* (2011) and this work's sample, the scatter is much more relevant than in the Ranalli *et al.* (2003) sample, which presents a tighter correlation. This would be expected if the X-ray luminosity in (U)LIRGS is not clearly dominated by binaries, but has multiple components in different proportions for each galaxy, and differently obscured.

In regards to future work, in order to further compare the correlations at low and high star formation rates, calculating the far infrared luminosity using (1) for the Iwasawa *et al.* (2011) sample would be an interesting addition. The derived AGN fraction for this sample ( $\sim 32\%$ ) is lower than for the high luminosity GOALS sample ( $\sim 50\%$ ), which could point towards a trend for AGN being more abundant towards higher luminosities. This could appear as further deviation from the correlation.

Another interesting addition in order to determine the origin of the X-ray emission for this work's sample would be the detection of the Fe line in the X-ray spectra, which would be incompatible with HMXB being the dominant source. This cannot be done through individual analysis of spectra for all galaxies, as photon counts are not high enough in most of the sources. However, there is a possibility to detect the existence of this line through stacking of the spectra of all sources, to obtain an averaged result, as has been previously done in Iwasawa *et al.* (2009).

## 5.2 Molecular disk and AGN interaction

As has been mentioned, most (U)LIRGs have quite dense and massive molecular disks surrounding the nucleus (e.g. Medling *et al.*, 2014; Scoville *et al.*, 2015; Xu *et al.*, 2015), absorbing the emission of both starburst and AGN components in X-rays. The masses of cold molecular gas can reach up to  $\sim 2 \cdot 10^{10} M_{\odot}$ , concentrated in the inner 1–3 kpc.

Since these sort of galaxies are the result of mergers or interactions, as described in 1.1.2, they are usually associated with starburst and AGN phenomena, making them ideal sites for the study of the interaction between the two processes. Conclusions from this work’s analysis also seem to point towards the existence of an obscured AGN in the nucleus of this type of galaxies. As the dense molecular gas is close to the nucleus, and therefore a starburst is taking place in the inner regions, there is a possibility of massive stars forming close to the nucleus and interfering with the AGN jets.

Jets are highly collimated, bipolar outflows coming from the centre of the AGN. The particles contained in this outflows, electrons, positrons and/or protons, are accelerated to very high energies, and in the presence of magnetic fields they give raise to non-thermal emission, thought to be mainly of synchrotron and inverse Compton origin. These jets may be very weak, or even absent in radio-quiet AGN, but in radio-loud sources powerful outflows can be ejected from the inner regions of the accretion disk, reaching distances between kpc and Mpc.

Massive stars produce powerful winds, which interact with the jet, forming a double bow shock. In addition, non-thermal emission can be generated: particles are accelerated to relativistic energies in the jet shock through Fermi-like acceleration mechanisms (Araudo *et al.* (2013)). High-energy emission is produced through electron and positron synchrotron emission and IC scattering of photons from the star, mainly (e.g. Mastichiadis and Kirk (1997)).

Taking as an example a massive disk with a scale height of 100 pc and an effective radius of 300 pc (similar to the 17 ULIRGs observed by Medling *et al.*, 2014), with most of the mass concentrated within these limits and distributed homogeneously, the number of stars formed per unit of mass can be calculated as a power-law mass distribution:  $\psi(m) \propto m^{-x}$ , with  $x \sim 2.3$  in the range  $0.1 < m/M_{\odot} < 120$  (Araudo *et al.*, 2013). For a disk-like region in an ULIRG, the star formation rate can be derived from the Schmidt law (Kennicutt, 1998) and the average cold molecular gas surface mass density, empirically determined (Bryant and Scoville, 1999). This allows the calculation of the power-law normalization.

Since stars are continuously dying, a lifetime for stars has to be considered:  $t_{life} = a(m/M_{\odot})^{-b}$  (Ekström *et al.*, 2012). Following the development in Araudo *et al.* (2013), we have reached the conclusion that the number of high-mass stars ( $8 < m/M_{\odot} < 120$ ) inside the jet at any given time is  $\sim 9000 \cdot (\theta/0.1)^2$ , where  $\theta$  is the half opening angle of the jet in radians.

As the stellar wind creates a double bow shock when in contact with the jet, at the contact discontinuity the shocked wind and the jet pressures are equal. The limit of the stellar wind's shocked and unshocked material, the wind bow shock, is located at a distance  $R_0$  of the centre of the star, defining a section  $\sigma_0 = \pi R_0^2$ , which is the section of interaction between jet and wind. It can be seen that this radius is  $R_0 = \sqrt{\dot{m}_* v_w c \pi} z t g \theta / 2 \sqrt{L_j}$ , where  $\dot{m}_*$  is the mass loss rate of the star,  $v_w$  the speed of its wind,  $z$  the height of the star within the jet, and  $L_j$  the jet's luminosity. However, simulations show that the value of this interaction radius is at least a factor of 6 larger (Bosch-Ramon, 2015). For the mass loss rate of the star, a simple expression such as  $\dot{m}_* = (m/120 M_\odot)^2 m/t_{life}$  is assumed, and common values are used for the rest of variables.

Integrating for the interaction section of all the stars within the jet, the conclusion reached is that approximately 1 % of the jet's surface at the limit of the molecular disk is intercepted by stellar interaction. We would then expect this interaction not to hinder significantly the jet as it advances through the medium.

Though it is clear that this development is a simplified approximation, with many assumptions (e.g. uniform distribution of stars within the jet, only main sequence stars considered, simple expression for the mass loss rate), it seems clear that there is a high number of massive stars within the jet at any time, and therefore there will be interaction.

A future interesting addition to this development would be, aside from improving the multiple approximations, calculating the non-thermal particle energy distribution and related radiation properties expected from the obtained stellar distribution within the jet. In this way it would be possible to estimate the amount of energy released by non-thermal processes in jet-star interactions, which would lead to determine if significant amounts of radiation are expected.

## References

- Araudo, A. T., Bosch-Ramon, V., and Romero, G. E. (2013). Gamma-ray emission from massive stars interacting with active galactic nuclei jets. *Monthly Notices of the RAS*, 436:3626–3639.
- Armus, L. et al. (2009). GOALS: The Great Observatories All-Sky LIRG Survey. *Publications of the ASP*, 121:559–576.
- Aschenbach, B. (1985). X-ray telescopes. *Reports on Progress in Physics*, 48:579–629.
- Barger, A. J., Cowie, L. L., and Wang, W.-H. (2007). The Microjansky Radio Galaxy Population. *Astrophysical Journal*, 654:764–781.
- Beckmann, V. and Shrader, C. R. (2012). *Active Galactic Nuclei*. ISBN-13: 978-3527410781.
- Bosch-Ramon, V. (2015). Non-thermal emission from standing relativistic shocks: an application to red giant winds interacting with AGN jets. *Astronomy and Astrophysics*, 575:A109.
- Bryant, P. M. and Scoville, N. Z. (1999). High-Resolution CO Observations of Luminous Infrared Galaxies. *Astronomical Journal*, 117:2632–2655.
- Crummy, J., Fabian, A. C., Gallo, L., and Ross, R. R. (2006). An explanation for the soft X-ray excess in active galactic nuclei. *Monthly Notices of the RAS*, 365:1067–1081.
- Dewangan, G. C., Griffiths, R. E., Rao, A., and Dasgupta, S. (2007). Time Lags in Narrow-Line Seyfert 1 Galaxies and the Origin of Their Soft Excess Emission. *Progress of Theoretical Physics Supplement*, 169:244–247.
- Done, C. (2007). The Origin of the Soft Excess in High  $L/L_{Edd}$  AGN. *Progress of Theoretical Physics Supplement*, 169:248–251.
- Downes, D. and Eckart, A. (2007). Black hole in the West nucleus of Arp 220. *Astronomy and Astrophysics*, 468:L57–L61.
- Ekström, S. et al. (2012). Grids of stellar models with rotation. I. Models from 0.8 to 120  $M_{\odot}$  at solar metallicity ( $Z = 0.014$ ). *Astronomy and Astrophysics*, 537:A146.
- Gandhi, P. (2005). X-ray studies of active galactic nuclei. *Asian Journal of Physics*, 13:90–107.
- George, I. M. and Fabian, A. C. (1991). X-ray reflection from cold matter in active galactic nuclei and X-ray binaries. *Monthly Notices of the RAS*, 249:352–367.
- Grimm, H.-J., Gilfanov, M., and Sunyaev, R. (2003). High-mass X-ray binaries as a star formation rate indicator in distant galaxies. *Monthly Notices of the RAS*, 339:793–809.
- Haardt, F. and Maraschi, L. (1993). X-ray spectra from two-phase accretion disks. *Astrophysical Journal*, 413:507–517.
- Hopkins, P. F. et al. (2005). Black Holes in Galaxy Mergers: Evolution of Quasars. *Astrophysical Journal*, 630:705–715.

- Hornschemeier, A. E. et al. (2005). Chandra-SDSS Normal and Star-Forming Galaxies. I. X-Ray Source Properties of Galaxies Detected by the Chandra X-Ray Observatory in SDSS DR2. *Astronomical Journal*, 129:86–103.
- Imanishi, M., Nakanishi, K., Tamura, Y., Oi, N., and Kohno, K. (2007). Millimeter Interferometric HCN(1-0) and HCO<sup>+</sup>(1-0) Observations of Luminous Infrared Galaxies. *Astronomical Journal*, 134:2366–2384.
- Iwasawa, K. et al. (2005). Fe K emission in the ultraluminous infrared galaxy Arp 220. *Monthly Notices of the RAS*, 357:565–571.
- Iwasawa, K. et al. (2009). High-Ionization Fe K Emission From Luminous Infrared Galaxies. *Astrophysical Journal, Letters*, 695:L103–L106.
- Iwasawa, K. et al. (2011). C-GOALS: Chandra observations of a complete sample of luminous infrared galaxies from the IRAS Revised Bright Galaxy Survey. *Astronomy and Astrophysics*, 529:A106.
- Kalberla, P. M. W. et al. (2005). The Leiden/Argentine/Bonn (LAB) Survey of Galactic HI. Final data release of the combined LDS and IAR surveys with improved stray-radiation corrections. *Astronomy and Astrophysics*, 440:775–782.
- Kauffmann, G. et al. (2003). The host galaxies of active galactic nuclei. *Monthly Notices of the RAS*, 346:1055–1077.
- Kennicutt, Jr., R. C. (1998a). Star Formation in Galaxies Along the Hubble Sequence. *Annual Review of Astron and Astrophys*, 36:189–232.
- Kennicutt, Jr., R. C. (1998b). The Global Schmidt Law in Star-forming Galaxies. *Astrophysical Journal*, 498:541–552.
- Lehmer, B. D. et al. (2008). Tracing the Mass-Dependent Star Formation History of Late-Type Galaxies using X-Ray Emission: Results from the Chandra Deep Fields. *Astrophysical Journal*, 681:1163–1182.
- Mastichiadis, A. and Kirk, J. G. (1997). Variability in the synchrotron self-Compton model of blazar emission. *Astronomy and Astrophysics*, 320:19–25.
- Medling, A. M. et al. (2014). Stellar and Gaseous Nuclear Disks Observed in Nearby (U)LIRGs. *Astrophysical Journal*, 784:70.
- Mewe, R., Kaastra, J. S., and Liedahl, D. A. (1995). Update of MEKA: MEKAL. *Legacy*, 6:16.
- Mineo, S. et al. (2014). X-ray emission from star-forming galaxies - III. Calibration of the L<sub>X</sub>-SFR relation up to redshift  $z \sim 1.3$ . *Monthly Notices of the RAS*, 437:1698–1707.
- Mould, J. R. et al. (2000). The Hubble Space Telescope Key Project on the Extragalactic Distance Scale. XXVIII. Combining the Constraints on the Hubble Constant. *Astrophysical Journal*, 529:786–794.
- Persic, M. and Rephaeli, Y. (2002). X-ray spectral components of starburst galaxies. *Astronomy and Astrophysics*, 382:843–859.

- Persic, M. and Rephaeli, Y. (2007). Galactic star formation rates gauged by stellar end-products. *Astronomy and Astrophysics*, 463:481–492.
- Petric, A. O. et al. (2011). Mid-Infrared Spectral Diagnostics of Luminous Infrared Galaxies. *Astrophysical Journal*, 730:28.
- Ranalli, P., Comastri, A., and Setti, G. (2003). The 2-10 keV luminosity as a Star Formation Rate indicator. *Astronomy and Astrophysics*, 399:39–50.
- Ricci, C. (2011). *Active Galactic Nuclei at hard X-ray energies: Absorption, Reflection and the Unified Model*. PhD thesis, ISDC, University of Geneva.
- Rumbaugh, N. et al. (2012). The Evolution and Environments of X-Ray Emitting Active Galactic Nuclei in High-redshift Large-scale Structures. *Astrophysical Journal*, 746:155.
- Sanders, D. B. (1999). The “Great Debate”: The case for AGNs. *Astrophysics and Space Science*, 266:331–348.
- Sanders, D. B. et al. (2003). The IRAS Revised Bright Galaxy Sample. *Astronomical Journal*, 126:1607–1664.
- Sanders, D. B. and Mirabel, I. F. (1996). Luminous Infrared Galaxies. *Annual Review of Astron and Astrophys*, 34:749.
- Schweitzer, M. et al. (2006). Spitzer Quasar and ULIRG Evolution Study (QUEST). I. The Origin of the Far-Infrared Continuum of QSOs. *Astrophysical Journal*, 649:79–90.
- Scoville, N. et al. (2015). ALMA Imaging of HCN, CS, and Dust in Arp 220 and NGC 6240. *Astrophysical Journal*, 800:70.
- Silverman, J. D. et al. (2009). The Environments of Active Galactic Nuclei within the zCOSMOS Density Field. *Astrophysical Journal*, 695:171–182.
- Stierwalt, S. et al. (2013). Mid-infrared Properties of Nearby Luminous Infrared Galaxies. I. Spitzer Infrared Spectrograph Spectra for the GOALS Sample. *Astrophysical Journal, Supplement*, 206:1.
- Wang, J. (2007). *An x-ray study of massive star forming regions with CHANDRA*. PhD thesis, The Pennsylvania State University.
- Xu, C. K. et al. (2015). ALMA Observations of Warm Dense Gas in NGC 1614-Breaking of the Star Formation Law in the Central Kiloparsec. *Astrophysical Journal*, 799:11.